Antarctic Ozone Loss Shapes Surface Cooling Pattern and Climate Sensitivity

Peidong Wang[a,b,#], Susan Solomon[b], Clara Deser[c], David W. J. Thompson[d,e], Noah S. Diffenbaugh[a]

[a]Doerr School of Sustainability, Stanford University, Stanford, CA, USA

[b]Department of Earth, Atmospheric, and Planetary Sciences, Massachusetts Institute of Technology, Cambridge, MA, USA

[c]Climate and Global Dynamics Laboratory, National Center for Atmospheric Research, Boulder, CO, USA

[d]Department of Atmospheric Science, Colorado State University, Fort Collins, CO, USA

[e]School of Environment Sciences, University of East Anglia, Norwich, UK

[#]Correspondence: Peidong Wang (pdwang@stanford.edu)

Changes in sea surface temperature (SST) patterns have been recognized as a major feedback affecting the sensitivity of climate to increases in greenhouse gases[1,2]. Over recent decades, while most of Earth's surface warmed, the eastern tropical Pacific and Southern Ocean unexpectedly cooled. These regional SST cooling are not quantitatively reproduced in global climate models (GCMs)[3], leading to systematic biases in estimates of global climate sensitivity[1,2]. While Antarctic ozone depletion has been proposed as a potential driver of the cooling[4], its influence has previously been considered too weak[5–7]. Here we provide novel evidence that suggests Antarctic ozone depletion can produce SST cooling that is comparable to the observed pattern and magnitude. Using ~4,000 years of simulation from eight GCMs, we construct a multiple linear regression model that isolates the intrinsic relationship between Antarctic ozone and SSTs, capturing robust short-timescale coupling while avoiding biases from the lack of resolved ocean eddies and their long-timescale adjustments[8–10]. We calculate that the ozone-driven SST pattern effect strengthened the global radiative feedback by up to 19% (0.7 W m^{-2} K^{-1}) during 1979-2000, thereby reducing effective climate sensitivity. As Antarctic ozone starts to recover[11,12], its stabilizing influence has begun to wane, leading to a more warming-prone climate.

Although GCMs capture the historical rise in global-mean surface temperature, they fail to reproduce some key spatial features—most notably the cooling trends in the eastern tropical Pacific and the Southern Ocean that have persisted over the past four decades[3] (Figure 1). This discrepancy between GCMs and observations exemplifies the SST

38 'pattern effect', in which the spatial pattern of SST influences the strength of climate
39 feedbacks and, in turn, the rate of global warming[13,14]. In particular, cooling in the eastern
40 tropical Pacific promotes low-cloud cover and enhances shortwave reflection, reducing
41 net radiative heating of the climate system[15]. Given the observed SST trend pattern,
42 recent decades exhibit more stabilizing climate feedbacks and are thus less prone to
43 warming, whereas GCMs lack this cooling pattern on average and therefore tend to have
44 less stabilizing climate feedbacks[2]. In addition, the observed eastern tropical Pacific
45 cooling may have influenced climate in remote regions through atmospheric
46 teleconnections, such as drought in the western United States[16]. Understanding the
47 observed SST cooling pattern is thus key for interpreting historical climate change,
48 assessing global climate sensitivity, and improving future global and regional climate
49 projections. However, the mechanisms responsible for this cooling signature remain
50 uncertain[17].
51
52 Antarctic ozone depletion has been proposed as a potential driver of Southern Ocean
53 SST cooling by strengthening and shifting the westerlies at high latitudes and thereby
54 altering wind-driven ocean circulation[4]. This poleward jet shift characterizes a transition
55 to the positive phase of the Southern Annular Mode (SAM) since the 1980s, driven largely
56 by Antarctic ozone depletion[18,19]. Despite this well-established mechanistic link, evidence
57 from empirical studies based on linear regression analysis[5], GCM experiments with
58 prescribed ozone forcing[6], and studies that convolve the Southern Ocean response with
59 observed ozone changes using idealized GCM ozone perturbation experiments[7]
60 suggests that ozone depletion explains less than 10% of the observed Southern Ocean

SST cooling in recent decades. However, these approaches have limitations that may lead to an underestimate of ozone's contribution. Decadal-scale variability of Southern Ocean SSTs is also influenced by response of the SAM to greenhouse gases[18,20,21] and is further complicated by remote influences from tropical Pacific SSTs via atmospheric teleconnections[22,23]. As a result, regressions based on short observational records may confound ozone's effects with other factors. In addition, standard-resolution GCMs (e.g., 1° horizontal resolution) tend to simulate a spurious enhancement of poleward ocean heat transport in response to an increase in the SAM on decadal timescales, inconsistent with both observations and results from high-resolution (e.g., 0.1° horizontal resolution) eddy-resolving ocean models[8–10,24]. This long-timescale warm bias arising from the lack of resolved ocean eddies in the Southern Ocean could substantially dampen the ozone-depletion-induced cooling signal in standard-resolution GCMs, leading to an underestimate of ozone's contribution. In principle, eddy-resolving ocean models could better represent the long-timescale Southern Ocean SST response to Antarctic ozone depletion. However, ozone-only single-forcing initial-condition large ensembles[25] with a sufficient number of members to cleanly isolate the forced response from internal variability have not yet been conducted with coupled ocean eddy-resolving models[26] due to their prohibitive computational cost. These limitations provide motivation to isolate the robust short-timescale response from the spurious long-timescale response when using standard-resolution GCMs to evaluate the role of Antarctic ozone depletion on Southern Ocean SST variability.

SST response to Antarctic ozone depletion

To characterize the simulated short-timescale intrinsic relationship between Antarctic ozone and SST, we construct a multiple linear regression (MLR) model in which annual-mean SST at each grid point is regressed onto the preceding year's (lag 1-year) September-December polar-cap (60°S-90°S) total column ozone using ~4,000 years of pre-industrial control (PiControl) simulations from eight GCMs archived in Phase 6 of the Coupled Model Intercomparison Project (CMIP6; Extended Data Table 1 and Methods). The selected GCMs employ either simplified or fully interactive stratospheric chemistry[27]. Therefore, despite their fixed pre-industrial levels of ozone-depleting substances, stratospheric ozone exhibits internally generated variability consistent with two-way coupling between ozone and atmospheric dynamics. The advantage of our methodology compared to regressions based on either observations or historical simulations is that the long PiControl simulations eliminate time-varying external forcings and span many phases of natural variability, enabling a rich sampling of the simulated ozone-SST relationship. This approach also isolates the surface temperature response to Antarctic ozone changes from the direct radiative forcing effects of global ozone and the ozone-depleting substances themselves. The disadvantage is that it relies on the fidelity of the simulated relationships between Antarctic ozone and SST, as well as on the assumption that the relationships derived from PiControl simulations remain valid under present-day conditions. Acknowledging GCM-specific biases, we establish robustness by considering only regions where all eight GCMs agree on the sign of the SST response to Antarctic ozone, with the spread of response magnitudes in these areas providing an estimate of inter-model uncertainty. Regression coefficients from individual GCMs and the multi-model-means for each predictor in the MLR are shown in Extended Data Figures 1-3.

Details of the MLR and additional sensitivity tests are provided in the Methods section and Extended Data Figure 4, including training the MLR on historical simulations or observations to assess whether the PiControl ozone-SST relationship holds under present-day conditions, and tests of ozone seasonality and its impact on SST.

To quantify SST responses to historical changes in Antarctic ozone, we apply the multi-model-mean intrinsic ozone-SST relationship derived from PiControl simulations to the satellite-observed Solar Backscatter Ultraviolet (SBUV[28]) ozone dataset. We then compare the inferred SST response against three widely used observation-based SST reconstructions from COBE-SST2 (ref.[29]), ERSSTv6 (refs.[30,31]), and HadISST1 (ref.[32]). The pattern and magnitude of the 1979-2024 SST cooling driven by changes in Antarctic ozone (Figure 1d) align remarkably well with the three observed SST reconstructions (Figures 1a-c) in the eastern tropical Pacific and Southern Ocean. Averaged over this region, where all eight GCMs exhibit a robust cooling response to declining Antarctic ozone (highlighted by dashed contours in Figures 1a-d), the ozone-explained SST cooling trend based on the MLR model is -0.067 ± 0.027 K dec^{-1} over 1979-2024 (±1σ of the MLR regression coefficients across the eight GCMs), while the three observational SST datasets yield cooling trends of -0.017 (COBE-SST2), -0.065 (ERSSTv6), and -0.042 (HadISST1) K dec^{-1}. The large inter-dataset spread likely reflects the sparse data coverage over the Southern Ocean, which can lead to substantial uncertainties[33]. Although this comparison is subject to important limitations, as observed SST reflects the combined influence of different external forcings and internal variability, it nevertheless

suggests that Antarctic ozone depletion alone can produce a cooling signal comparable in magnitude to the observed change over the past four decades.

The observed 22-year running mean Antarctic ozone time series (red curve in Figure 1f) exhibits a pronounced decline from ~1979 to 2000 during the ozone depletion era, followed by a plateau in the recovery period after 2000. Figure 1f also presents the 22-year running-mean SST anomalies from both the observations and predicted by the MLR from the observed ozone time series, averaged over the dashed region in Figures 1a-d. (The unfiltered and 22-year running mean SST anomalies averaged separately over the eastern tropical Pacific and Southern Ocean are shown in Extended Data Figure 5.) As expected, the regional-mean ozone-explained SSTs from the MLR model (blue curve) mirror the Antarctic ozone time series, showing a rapid cooling from 1979 to 2000 followed by steady conditions thereafter. However, given the large inter-dataset uncertainties and the influence of interannual and decadal SST variability unrelated to Antarctic ozone, it remains challenging to robustly identify a transition from cooling to steady conditions in the observed SST records across the pre- and post-2000 periods.

Previous studies have suggested that Antarctic ozone depletion can produce a broad spatial pattern of cooling that resembles observations, but the simulated response is typically an order of magnitude weaker than observed[5,6]. This raises the question: why can the MLR model, trained on the linkages between Antarctic ozone and SSTs in PiControl simulations, capture the observed magnitude of eastern tropical Pacific and Southern Ocean SST cooling? Studies using standard-resolution GCMs generally find

that the Southern Ocean cools in response to an increase in the SAM on short (i.e., annual) timescales but warms on long (i.e., multi-annual and decadal) timescales[7,21,34]. In contrast, recent high-resolution, eddy-resolving ocean models show a consistent short-timescale cooling response but no evidence of significant long-timescale warming response, possibly owing to mesoscale eddy compensation that suppresses the interior upwelling of warm deep water[8]. Consistent with this difference, fully eddy-resolving GCMs simulate substantially less Southern Ocean SST warming on decadal timescales in response to SAM increases than their standard-resolution counterparts (see Extended Data Figure 6 and Methods). This distinction is also evident in ocean heat transport, with standard-resolution GCMs exhibiting long-timescale enhanced poleward heat transport in response to an increase in the SAM, opposite to the trends seen in eddy-resolving models and observations[8–10,24]. By regressing SST on the preceding year's Antarctic ozone, our MLR model primarily captures the short-timescale ozone-SST coupling dominated by wind-driven Ekman heat transport, which is well represented in standard-resolution GCMs and supported by observations[8], while excluding the spurious long-timescale response associated with the absence of resolved ocean eddies.

The short-timescale coupling between Antarctic ozone and SSTs in the PiControl simulations is evident in lead-lag composites of sea-level pressure (SLP) and 500-hPa geopotential heights (Z500) between low (<10th percentile) and moderate (40th-60th percentile) Antarctic ozone years (Figure 2). Antarctic ozone variability in PiControl simulations arises primarily from the El Niño–Southern Oscillation (ENSO): El Niño/La Niña accelerates/slows the Brewer-Dobson circulation in the stratosphere, transporting

more/less ozone-rich air poleward[35], with ENSO leading Antarctic ozone by ~12 months[36]. Consistent with this mechanism, composite SST anomalies one year before low Antarctic ozone show pronounced La Niña-like cooling in the tropical Pacific (Figure 2a). The accompanying SLP and Z500 anomaly patterns—enhanced west-east tropical Indo-Pacific SLP gradient and broad tropical-mean reduction in Z500 (Figures 2d,g)—likewise reflect the canonical ENSO-troposphere coupling[37,38]. Once La Niña establishes anomalously low Antarctic ozone during austral spring (September-December), ozone exerts its strongest influence on Southern Hemisphere climate in the following summer (January-April). The resulting patterns resemble the positive phase of the SAM, featuring stronger meridional SLP and Z500 gradients associated with a poleward-shifted jet that intensifies equatorward Ekman heat transport, leading to SST cooling in the Southern Ocean[18] (Figures 2b,e,h). Cold air originating over the Southern Ocean is advected equatorward and subsequently amplified and sustained by positive feedbacks in both the atmosphere and the ocean along the west coast of South America, thereby reinforcing cooling in the southeast and eastern tropical Pacific[39,40].

Impact on historical climate sensitivity

'Pattern effects' associated with the spatial structure of SST trends, including cooling in the eastern tropical Pacific and Southern Ocean, have slowed global warming during the historical period[2,41]. To quantify the contribution of Antarctic ozone depletion and recovery to these pattern effects, we apply a Green's Function approach[1,15,42] to estimate the temporal evolution of the global radiative feedback parameter associated with the ozone-induced component of observed SST trends (see Methods). Figure 3 shows the percent

198 contribution from ozone-induced changes in the pattern of SST trends for top-of-
199 atmosphere net radiation (R; negative values indicate outgoing radiation), global-mean
200 surface temperature (T), and the global radiative feedback parameter ($\lambda = R/T$) computed
201 from overlapping 22-year SST trend windows. The corresponding absolute contributions
202 are shown in Extended Data Figure 7.
203
204 During 1979-2000, when Antarctic ozone depletion was strongest, the resulting ozone-
205 induced SST cooling based on the MLR model was also largest in the eastern tropical
206 Pacific (Extended Data Figure 5b), where radiative feedbacks are particularly
207 sensitive[1,15,42,43]. We estimate that the ozone-induced SST trend pattern during this period
208 increased radiative cooling to space by 2-6% (6.1-20.2 mW m^{-2} dec^{-1}), with the range
209 representing the spread in mean estimates across different Green's functions (see
210 Methods). At the same time, the ozone-induced SST trend pattern reduced the rate of
211 global surface warming by 7-18% (0.01-0.02 K dec^{-1}). Together, these effects produced
212 an 8-19% (0.21-0.70 W m^{-2} K^{-1}) strengthening of the global radiative feedback (i.e.,
213 making λ more negative). In other words, the SST trend pattern induced by ozone
214 depletion enhanced radiative damping, leading to more energy lost to space per degree
215 of surface warming and a more stable, less warming-prone climate state.
216
217 **SST pattern effect under ozone recovery**
218 When the analysis is extended into the 21st-century ozone recovery period, the ozone-
219 induced SST cooling in the eastern tropical Pacific becomes weaker and can even
220 reverse sign (Extended Data Figure 5b). As a result, ozone's contribution to enhanced

radiative cooling correspondingly diminishes, and global-mean surface warming accelerates. This shift yields a less stable, more warming-prone climate state, reflected in a positive change in λ for periods beginning after the mid-1990s (Figure 3). Notably, the time-varying climate sensitivity we diagnose from ozone-induced SST pattern changes closely matches the behavior reported in ref.[2], which identifies a substantially lower-sensitivity state emerging after the 1980s relative to that expected from long-term CO_2 increases, followed by a gradual waning of this difference after the 2000s.

Due to declines in ozone-depleting substances, signs of Antarctic ozone recovery have already emerged in the 21st century[11,12]. However, because of the large natural variability in ozone and the short observational record, along with the exceptional 2020 Australian wildfires and the 2022 Hunga-Tonga volcanic eruption that contributed to additional ozone losses[44,45], the SSTs explained by observed ozone according to our MLR method still show a weak cooling trend in the eastern tropical Pacific and Southern Ocean during 2000-2024 (Figure 4a). In contrast, GCM-simulated ozone, which combines historical and scenario (SSP2-4.5) forcings and does not include the recent exceptional wildfire- and volcano-driven ozone losses (see Methods), yields a reversal in sign of the MLR-derived SST trends during 2000-2024 (i.e., a warming pattern in the eastern tropical Pacific and Southern Ocean; Figures 4b-c).

Under the SSP2-4.5 scenario, Antarctic ozone is projected to return to 1980 levels by the middle of the 21st century[27], implying that the SST cooling in the eastern tropical Pacific and Southern Ocean induced by ozone depletion and the associated shift toward a more

negative global radiative feedback should likewise subside by the 2050s, all other factors being equal (Figure 4c). Note that the SST projections in Figure 4c reflect only the response to changes in Antarctic ozone. As ozone recovery proceeds more gradually than the preceding rapid depletion, future changes in other factors such as anthropogenic aerosols[46,47], greenhouse gases[48], and Antarctic ice-sheet melt[49] may increasingly dominate SST evolution and influence the timing of the 'de-emergence' of the SST pattern effect associated with Antarctic ozone recovery.

Summary and conclusions

In summary, we provide numerical evidence that suggests Antarctic ozone depletion can produce SST cooling in the eastern tropical Pacific and Southern Ocean that is comparable to the observed magnitude. This evidence is based on a MLR model developed from the statistics of interannual ozone-SST dynamical coupling in unforced (PiControl) simulations, which avoids biases arising from unresolved ocean eddy adjustments on longer timescales in standard-resolution GCMs. We find that both the spatial structure and magnitude of this short-timescale intrinsic ozone-SST relationship are robust across PiControl simulations, historical simulations, and observations. However, because long-timescale responses remain highly model dependent even in eddy-resolving ocean models[8–10,50], and observational records are too short to constrain their magnitude[8], our focus on the short-timescale response should be interpreted as a physically motivated upper-bound estimate of ozone-driven SST changes.

We also estimate that this ozone-depletion-induced SST trend pattern has contributed to a decrease in global climate sensitivity in recent decades, with the strongest effect during 1979-2000, strengthening the global radiative feedback by 8-19%. Likewise, if Antarctic ozone continues to recover from its minimum around the turn of the 21st century, the global radiative feedback is expected to shift toward a higher-sensitivity, more warming-prone climate. In this context, it is important to emphasize that the climate sensitivity results presented here isolate only the ozone-induced SST pattern effect and do not represent the full range of radiative, chemical, and dynamical benefits associated with ozone recovery, which remain essential for climate and environmental protection. More broadly, these findings highlight Antarctic ozone as a key regulator of global climate through its impact on SST pattern effects, and underscore the importance of representing chemistry-climate interactions in the coupled stratosphere-troposphere-ocean system for improved understanding of historical and future climate change.

References

1. Dong, Y., Proistosescu, C., Armour, K. C. & Battisti, D. S. Attributing Historical and Future Evolution of Radiative Feedbacks to Regional Warming Patterns using a Green's Function Approach: The Preeminence of the Western Pacific. *Journal of Climate* **32**, 5471–5491 (2019).
2. Andrews, T. *et al.* On the Effect of Historical SST Patterns on Radiative Feedback. *Journal of Geophysical Research: Atmospheres* **127**, e2022JD036675 (2022).
3. Wills, R. C. J., Dong, Y., Proistosecu, C., Armour, K. C. & Battisti, D. S. Systematic Climate Model Biases in the Large-Scale Patterns of Recent Sea-Surface

Temperature and Sea-Level Pressure Change. *Geophysical Research Letters* **49**, e2022GL100011 (2022).

4. Hartmann, D. L. The Antarctic ozone hole and the pattern effect on climate sensitivity. *Proceedings of the National Academy of Sciences* **119**, e2207889119 (2022).
5. Dong, Y., Polvani, L. M. & Bonan, D. B. Recent Multi-Decadal Southern Ocean Surface Cooling Unlikely Caused by Southern Annular Mode Trends. *Geophysical Research Letters* **50**, e2023GL106142 (2023).
6. Dong, Y., Polvani, L. M., Hwang, Y.-T. & England, M. R. Stratospheric ozone depletion has contributed to the recent tropical La Niña-like cooling pattern. *npj Climate and Atmospheric Science* **8**, 150 (2025).
7. Seviour, W. J. M. *et al.* The Southern Ocean Sea Surface Temperature Response to Ozone Depletion: A Multimodel Comparison. *Journal of Climate* **32**, 5107–5121 (2019).
8. Doddridge, E. W. *et al.* Eddy Compensation Dampens Southern Ocean Sea Surface Temperature Response to Westerly Wind Trends. *Geophysical Research Letters* **46**, 4365–4377 (2019).
9. Bilgen, S. I. & Kirtman, B. P. Impact of ocean model resolution on understanding the delayed warming of the Southern Ocean. *Environmental Research Letters* **15**, 114012 (2020).
10. Yeager, S. G. *et al.* Reduced Southern Ocean warming enhances global skill and signal-to-noise in an eddy-resolving decadal prediction system. *npj Climate and Atmospheric Science* **6**, 107 (2023).

11. Solomon, S. *et al.* Emergence of healing in the Antarctic ozone layer. *Science* **353**, 269–274 (2016).
12. Wang, P. *et al.* Fingerprinting the recovery of Antarctic ozone. *Nature* **639**, 646–651 (2025).
13. Stevens, B., Sherwood, S. C., Bony, S. & Webb, M. J. Prospects for narrowing bounds on Earth's equilibrium climate sensitivity. *Earth's Future* **4**, 512–522 (2016).
14. Armour, K. C., Bitz, C. M. & Roe, G. H. Time-Varying Climate Sensitivity from Regional Feedbacks. *Journal of Climate* **26**, 4518–4534 (2013).
15. Zhou, C., Zelinka, M. D. & Klein, S. A. Analyzing the dependence of global cloud feedback on the spatial pattern of sea surface temperature change with a Green's function approach. *Journal of Advances in Modeling Earth Systems* **9**, 2174–2189 (2017).
16. Seager, R. *et al.* Causes of the 2011–14 California Drought. *Journal of Climate* **28**, 6997–7024 (2015).
17. Watanabe, M. *et al.* Possible shift in controls of the tropical Pacific surface warming pattern. *Nature* **630**, 315–324 (2024).
18. Thompson, D. W. J. *et al.* Signatures of the Antarctic ozone hole in Southern Hemisphere surface climate change. *Nature Geoscience* **4**, 741–749 (2011).
19. Polvani, L. M., Waugh, D. W., Correa, G. J. P. & Son, S.-W. Stratospheric Ozone Depletion: The Main Driver of Twentieth-Century Atmospheric Circulation Changes in the Southern Hemisphere. *Journal of Climate* **24**, 795–812 (2011).
20. Arblaster, J. M. & Meehl, G. A. Contributions of External Forcings to Southern Annular Mode Trends. *Journal of Climate* **19**, 2896–2905 (2006).

21. Kostov, Y., Ferreira, D., Armour, K. C. & Marshall, J. Contributions of Greenhouse Gas Forcing and the Southern Annular Mode to Historical Southern Ocean Surface Temperature Trends. *Geophysical Research Letters* **45**, 1086–1097 (2018).
22. Schneider, D. P., Deser, C. & Fan, T. Comparing the Impacts of Tropical SST Variability and Polar Stratospheric Ozone Loss on the Southern Ocean Westerly Winds. *Journal of Climate* **28**, 9350–9372 (2015).
23. Watanabe, M., Dufresne, J.-L., Kosaka, Y., Mauritsen, T. & Tatebe, H. Enhanced warming constrained by past trends in equatorial Pacific sea surface temperature gradient. *Nature Climate Change* **11**, 33–37 (2021).
24. Armour, K. C., Marshall, J., Scott, J. R., Donohoe, A. & Newsom, E. R. Southern Ocean warming delayed by circumpolar upwelling and equatorward transport. *Nature Geoscience* **9**, 549–554 (2016).
25. Deser, C. *et al.* Isolating the Evolving Contributions of Anthropogenic Aerosols and Greenhouse Gases: A New CESM1 Large Ensemble Community Resource. *Journal of Climate* **33**, 7835–7858 (2020).
26. Dhame, S., Olonscheck, D. & Rugenstein, M. Higher-Resolution Climate Models Do Not Consistently Reproduce the Observed Tropical Pacific Warming Pattern. *Journal of Climate* **38**, 3131–3149 (2025).
27. Keeble, J. *et al.* Evaluating stratospheric ozone and water vapour changes in CMIP6 models from 1850 to 2100. *Atmospheric Chemistry and Physics* **21**, 5015–5061 (2021).

28. McPeters, R. D., Bhartia, P. K., Haffner, D., Labow, G. J. & Flynn, L. The version 8.6 SBUV ozone data record: An overview. *Journal of Geophysical Research: Atmospheres* **118**, 8032–8039 (2013).
29. Hirahara, S., Ishii, M. & Fukuda, Y. Centennial-Scale Sea Surface Temperature Analysis and Its Uncertainty. *Journal of Climate* **27**, 57–75 (2014).
30. Huang, B. *et al.* Extended Reconstructed Sea Surface Temperature, Version 6 (ERSSTv6). Part I: An Artificial Neural Network Approach. *Journal of Climate* **38**, 1105–1121 (2025).
31. Huang, B. *et al.* Extended Reconstructed Sea Surface Temperature, Version 6 (ERSSTv6). Part II: Upgrades on Quality Control and Large-Scale Filter. *Journal of Climate* **38**, 1123–1136 (2025).
32. Rayner, N. A. *et al.* Global analyses of sea surface temperature, sea ice, and night marine air temperature since the late nineteenth century. *Journal of Geophysical Research: Atmospheres* **108**, (2003).
33. Cooper, V. T., Hakim, G. J. & Armour, K. C. Monthly Sea Surface Temperature, Sea Ice, and Sea Level Pressure over 1850–2023 from Coupled Data Assimilation. *Journal of Climate* **38**, 5461–5490 (2025).
34. Ferreira, D., Marshall, J., Bitz, C. M., Solomon, S. & Plumb, A. Antarctic Ocean and Sea Ice Response to Ozone Depletion: A Two-Time-Scale Problem. *Journal of Climate* **28**, 1206–1226 (2015).
35. Calvo, N., Garcia, R. R., Randel, W. J. & Marsh, D. R. Dynamical Mechanism for the Increase in Tropical Upwelling in the Lowermost Tropical Stratosphere during Warm ENSO Events. *Journal of the Atmospheric Sciences* **67**, 2331–2340 (2010).

36. He, H. *et al.* Lagged ENSO teleconnection mechanisms driving Antarctic stratospheric ozone depletion variability. *Atmospheric Research* **329**, 108539 (2026).
37. Trenberth, K. E. & Smith, L. The Vertical Structure of Temperature in the Tropics: Different Flavors of El Niño. *Journal of Climate* **19**, 4956–4973 (2006).
38. Bjerknes, J. Atmospheric Teleconnections from the Equatorial Pacific. *Monthly Weather Review* **97**, 163–172 (1969).
39. Kim, H., Kang, S. M., Kay, J. E. & Xie, S.-P. Subtropical clouds key to Southern Ocean teleconnections to the tropical Pacific. *Proceedings of the National Academy of Sciences* **119**, e2200514119 (2022).
40. Dong, Y., Armour, K. C., Battisti, D. S. & Blanchard-Wrigglesworth, E. Two-Way Teleconnections between the Southern Ocean and the Tropical Pacific via a Dynamic Feedback. *Journal of Climate* **35**, 6267–6282 (2022).
41. Armour, K. C. *et al.* Sea-surface temperature pattern effects have slowed global warming and biased warming-based constraints on climate sensitivity. *Proceedings of the National Academy of Sciences* **121**, e2312093121 (2024).
42. Zhang, B., Zhao, M. & Tan, Z. Using a Green's Function Approach to Diagnose the Pattern Effect in GFDL AM4 and CM4. *Journal of Climate* **36**, 1105–1124 (2023).
43. Alessi, M. J. & Rugenstein, M. A. A. Surface Temperature Pattern Scenarios Suggest Higher Warming Rates Than Current Projections. *Geophysical Research Letters* **50**, e2023GL105795 (2023).
44. Solomon, S. *et al.* Chlorine activation and enhanced ozone depletion induced by wildfire aerosol. *Nature* **615**, 259–264 (2023).

45. Wang, X. *et al.* Stratospheric Climate Anomalies and Ozone Loss Caused by the Hunga Tonga-Hunga Ha'apai Volcanic Eruption. *Journal of Geophysical Research: Atmospheres* **128**, e2023JD039480 (2023).
46. Smith, D. M. *et al.* Role of volcanic and anthropogenic aerosols in the recent global surface warming slowdown. *Nature Climate Change* **6**, 936–940 (2016).
47. Hwang, Y.-T., Xie, S.-P., Chen, P.-J., Tseng, H.-Y. & Deser, C. Contribution of anthropogenic aerosols to persistent La Niña-like conditions in the early 21st century. *Proceedings of the National Academy of Sciences* **121**, e2315124121 (2024).
48. Seager, R. *et al.* Strengthening tropical Pacific zonal sea surface temperature gradient consistent with rising greenhouse gases. *Nature Climate Change* **9**, 517–522 (2019).
49. Schloesser, F., Friedrich, T., Timmermann, A., DeConto, R. M. & Pollard, D. Antarctic iceberg impacts on future Southern Hemisphere climate. *Nature Climate Change* **9**, 672–677 (2019).
50. Bitz, C. M. & Polvani, L. M. Antarctic climate response to stratospheric ozone depletion in a fine resolution ocean climate model. *Geophysical Research Letters* **39**, (2012).

Methods

Observation and model descriptions

We consider three widely used, global, gridded SST datasets from 1979 to 2024: the Japan Meteorological Agency Centennial Observation-Based Estimates of SSTs (COBE-

SST2; ref.[29]), the U.S. National Oceanic and Atmospheric Administration Extended Reconstructed SST (ERSSTv6; refs.[30,31]), and the U.K. Met Office Hadley Centre Sea Ice and Sea Surface Temperature dataset (HadISST1; ref.[32]). These datasets are reconstructed primarily from *in situ* ship and buoy measurements, with HadISST1 further supplemented by satellite observations after the 1980s. The Southern Ocean remains the region with the sparsest observational coverage, even after 1980 (ref.[33]), resulting in substantial inter-dataset uncertainties. To account for this observational uncertainty, we include all three reconstructed SST products in our analysis.

We consider satellite observations of total column ozone from the Solar Backscatter Ultraviolet (SBUV) version 8.7 (ref.[28]), which provides a monthly and zonally averaged ozone dataset from 1970 to 2023. We use the period from 1978 to 2023 to predict ozone-explained SSTs for the period from 1979 to 2024. The SBUV observations have been validated against ground-based Dobson and Brewer measurements and are widely used in past ozone assessments to characterize long-term global and polar ozone changes[51,52].

The models used to construct the MLR in this study are based on PiControl simulations from eight CMIP6 GCMs that employ either simplified or fully interactive stratospheric chemistry schemes. For consistency, we use 499 years from each GCM, although some (e.g., MRI-ESM2-0 and UKESM1-0-LL) provide longer PiControl simulations. To remove any potential model drifts in the PiControl simulations, all variables are linearly detrended on a monthly basis at each grid point. We also use one realization from each GCM's historical simulation (up to 2014) and the SSP2-4.5 scenario (after 2014) in certain

447 analyses (Figures 1e and 4b,c). Since two of the eight GCMs do not provide SSP
448 simulations, the multi-model-mean after 2014 is calculated from the remaining six models.
449 For the MLR sensitivity test shown in Extended Data Figure 4f, we use all realizations
450 from the historical simulations of CNRM-CM6-1, CNRM-ESM2-1, MRI-ESM2-0, and
451 UKESM1-0-LL for the period 1975-2014. The list of GCMs used is summarized in
452 Extended Data Table 1, and additional details, including their respective chemistry
453 schemes, are provided in ref.[27].
454
455 Unless otherwise specified, all spatial averages presented in this study are weighted by
456 the cosine of latitude to account for variations in grid-cell area across latitude.
457
458 **Multiple linear regression and sensitivity tests**
459 We construct the following MLR for each CMIP6 GCM using its 499 years of PiControl
460 simulations to characterize the intrinsic relationship between Antarctic ozone and SST:

$$SST(i,j,t) = \alpha(i,j) \cdot Ozone(t-1) + \beta_1(i,j) \cdot ENSO(t-1) + \beta_2(i,j) \cdot ENSO(t) + \epsilon \qquad (1)$$

461 where the annual-mean SST anomaly at each grid point (*i*,*j*) in year *t* is regressed onto
462 September-December total column ozone anomaly averaged over 60°S-90°S from the
463 preceding year (*t*-1), and the ENSO indices, calculated as annual-mean SST anomalies
464 averaged over the Niño 3.4 region (5°N-5°S, 170°W-120°W) in years *t*-1 and *t*. Integrated
465 total column ozone is used here because it primarily reflects ozone variability in the lower
466 stratosphere, consistent with the altitude range where present-day ozone depletion
467 dominates[53]. Accordingly, the surface impact associated with lower-than-normal column
468 ozone in PiControl simulations exhibits behavior consistent with our understanding of the
469 surface response to present-day Antarctic ozone depletion[18] (Figure 2). The observed

Antarctic ozone change over the past four decades falls reasonably within the distribution of internal variability simulated in the PiControl runs (Extended Data Figure 8). ENSO indices are included as additional predictors because Antarctic ozone variability is partly modulated by ENSO teleconnections[54], which also influence global SST directly, with ENSO leading SST by about 0-1.5 years[55]. Including both lag 1-year and lag 0-year ENSO indices allows the partial regression coefficient on Antarctic ozone to capture, as far as possible, the local ozone influence on SST.

Given differences in model physics, some GCMs (e.g., CNRM-CM6-1 and E3SM-1-0) exhibit a stronger SST response to Antarctic ozone, whereas others (e.g., GFDL-ESM4) show a weaker response, as illustrated by the partial regression coefficients for Antarctic ozone in individual GCMs (Extended Data Figures 1a-h). Our analysis focuses on regions where all eight GCMs agree on the sign of the SST response to Antarctic ozone, highlighted by dashed contours in the multi-model-mean (Extended Data Figure 1i). We also include ±1σ of the multi-model-mean coefficients to represent uncertainty associated with GCM differences. Applying this criterion, the eastern tropical Pacific and the Southern Ocean both emerge as regions with a robust SST response to Antarctic ozone variability. In both regions, all GCMs yield positive coefficients, indicating SST cooling with Antarctic ozone depletion (i.e., lower ozone). The warming in the South Indian Ocean (in response to a decrease in Antarctic ozone) and the dipole pattern in the South Atlantic Ocean are also consistent with SAM-based regression from observations[4]. Importantly, this robust inter-model agreement between Antarctic ozone and SST is largely confined to the

492 Southern Hemisphere, suggesting that ENSO teleconnections are effectively minimized
493 in the partial regression on Antarctic ozone.
494
495 We conduct additional sensitivity tests to examine the robustness and physical linkage
496 between Antarctic ozone and SST. The key relationship between Antarctic ozone loss
497 during springtime and lower-than-normal SSTs in the eastern tropical Pacific and the
498 Southern Ocean is both robust across different analysis designs and consistent with
499 physical expectations. For instance, similar patterns and magnitudes emerge in MLR
500 analyses using Antarctic ozone averaged in September-October (Extended Data Figure
501 4a) and November-December (Extended Data Figure 4b). In contrast, this relationship
502 disappears when using Antarctic ozone averaged in March-April (Extended Data Figure
503 4c), when the stratospheric polar vortex has largely broken down and ozone variability is
504 no longer dynamically coupled to the tropospheric circulation[56]. We further test a simple
505 linear regression between Antarctic ozone and SST, and the magnitude of the cooling
506 over the eastern tropical Pacific and the Southern Ocean remains comparable to that
507 obtained from the MLR (Extended Data Figure 4d), underscoring the robustness of the
508 ozone-SST relationship in these regions.
509
510 We further test whether the PiControl ozone-SST relationship holds under present-day
511 conditions by constructing an MLR using both observations (based on data from 1979-
512 2022) and CMIP6 historical simulations (based on model outputs from 1975-2014).
513 Because observations can conflate forced responses and internal variability, we first
514 remove the forced component from observed SST, estimated as the average of the top

five most skillful methods evaluated in the Forced Component Estimation Statistical Method Intercomparison Project (ForceSMIP[57]). We then apply the MLR between observed ozone (from SBUV) and the SST internal variability (with the forced component removed from ERSSTv5); the resulting ozone-driven SST trend is shown in Extended Data Figure 4e. Additionally, we construct the MLR based on internal variability in a subset of four GCMs from Extended Data Table 1 (CNRM-CM6-1, CNRM-ESM2-1, MRI-ESM2-0 and UKESM1-0-LL), each of which provides at least 10 historical realizations. By removing the ensemble mean from each realization, the residual largely reflects internal variability. The resulting SST trend from MLR based on these historical simulations is shown in Extended Data Figure 4f. Hatching in the eastern tropical Pacific and Southern Ocean in both Extended Data Figures 4e and 4f indicates that the ozone-driven cooling derived from internal variability in either observations or historical simulations is consistent with the PiControl ozone-SST relationship, falling within the ±1σ inter-model uncertainty.

Climate response function calculation

Following refs.[7,58], we estimate the Southern Ocean SST response to a step increase in the SAM index using control simulations from five GCMs participating in the High Resolution Model Intercomparison Project (HighResMIP[59]). These GCMs provide paired standard- and high-resolution configurations, each spanning approximately 100 years, enabling a comparison of SST responses across resolutions without confounding differences in model physics.

538 The Southern Ocean SST anomalies can be represented as a convolution of impulse
539 response functions G with respect to the SAM index. A discretized form of this integral is
540 given by:

$$SST(t) \approx \sum_{\tau=0}^{\tau_{max}} G(\tau) \cdot SAM(t-\tau) \cdot \Delta\tau + \epsilon \quad (2)$$

541 where the Southern Ocean SST is the annual-mean SST averaged over 50°S-70°S, and
542 SAM is the December-May averaged SAM index, calculated as the monthly normalized
543 SLP difference between 40°S and 65°S. These definitions follow ref.[7], which shows that
544 SST responses to SAM estimated in this way provide a good proxy for the responses to
545 Antarctic ozone depletion. The lag τ is measured in years with a time increment $\Delta\tau$ = 1
546 year. The response function G is then estimated using MLR of Southern Ocean SST
547 anomaly onto SAM indices at various time lags. To reduce sensitivity to fitting choices,
548 we average results across a range of fitting parameter spaces[58]. Specifically, the
549 maximum lag cutoff τ_{max} is varied from 55 to 75 years in 5-year increments, and the full
550 time series is truncated by 0-10% at both the beginning and end in 2% increments. The
551 climate response function (CRF) of the Southern Ocean SST t years after a 1σ step
552 increase in SAM is then estimated as:

$$CRF(t) = \sum_{\tau=0}^{t} G(\tau) \cdot \Delta\tau \quad (3)$$

553

554 Earlier studies calculating CRFs from standard-resolution GCMs generally find that
555 Southern Ocean SST cools in response to a positive SAM anomaly on short timescales
556 but warms on longer timescales, although the magnitude of long-term warming is highly

uncertain and model dependent[7,21,58]. Extended Data Figure 6 shows the difference in CRFs between the high- and standard-resolution configurations for each HighResMIP GCM, illustrating how the Southern Ocean SST response changes with increased model resolution. For CESM1-CAM5 and HadGEM3-GC31, whose high-resolution ocean grids are finer than 0.1°, the minimum resolution required to fully resolve mesoscale ocean eddies[60], their high-resolution configurations exhibit substantially weaker long-timescale warming than their standard-resolution counterparts. Although CNRM-CM6-1 and ECMWF-IFS show mixed or even opposite behavior, their high-resolution configurations adopt a 0.25° ocean grid, which may still be too coarse to fully resolve mesoscale ocean eddies[60,61].

Greens function approach for climate sensitivity analysis

The Green's function approach enables us to quantify how a given SST pattern modulates the global climate feedback[1,15,42], defined as the global radiative response per degree of global-mean surface temperature change:

$$\lambda = \frac{R}{T} = \frac{\sum_{i,j} GF_R(i,j) \cdot SST_{trend}(i,j)}{\sum_{i,j} GF_T(i,j) \cdot SST_{trend}(i,j)} \quad (4)$$

where R and T represent the trends in top-of-atmosphere net radiation (units in W m^{-2} dec^{-1}) and global-mean surface temperature (units in K dec^{-1}), obtained by integrating the Green's functions for radiation (GF_R) and surface temperature (GF_T) with a given SST trend pattern (SST_{trend}) globally. The resulting λ (units in W m^{-2} K^{-1}) represents the global radiative feedback associated with the SST trend pattern over the given trend period.

578 The Green's functions used in this study are derived from CESM1-CAM4 (ref.[1]), CESM1-
579 CAM5 (ref.[15]), and GFDL-AM4 (ref.[42]) to estimate the range of uncertainty arising from
580 differences in model physics. To ensure consistent spatial integration, all datasets
581 (including observations, CMIP6 outputs, and the Green's functions) are first re-gridded to
582 the horizontal resolution of CESM1-CAM4 (approximately 1.9° × 2.5°). Note that sea ice
583 pattern effects can also play an important role in the global energy budget[62]. Among the
584 models considered here, only CESM1-CAM4 includes the effects of sea ice changes[1],
585 whereas the others mainly prescribe sea ice. This difference may partly explain why the
586 changes in R, T, and λ associated with Antarctic ozone are more pronounced when using
587 the Green's function from CESM1-CAM4 (Figure 3 and Extended Data Figure 7).
588
589 We apply a sliding 22-year trend window from 1979 to 2024 to capture the gradual
590 transition from the ozone-depletion era (mainly 1979-2000) to the ozone-recovery era
591 (after 2000). We calculate R, T, and λ for the observed SST trend patterns using three
592 observation-based SST datasets (COBE-SST2, ERSSTv6, HadISST1), representing
593 real-world trends that include both external forcings and internal variability. For each
594 observed SST dataset, we also subtract the ozone-explained SST component to estimate
595 R, T, and λ representing a hypothetical world without ozone-induced SST changes. The
596 subtraction is applied only over regions where all eight GCMs agree on the sign of the
597 SST response to Antarctic ozone (dashed regions in Extended Data Figure 1i), including
598 robust SST cooling in the eastern tropical Pacific and the Southern Ocean and warming
599 in the South Indian Ocean and South Atlantic Ocean due to Antarctic ozone depletion.
600 The resulting differences in R, T, and λ between those derived from observed SST and

those derived from observed SST with the ozone-explained component removed represent the contribution of Antarctic ozone changes. The relative contributions are shown in Figure 3, and the absolute contributions are shown in Extended Data Figure 7.

Additional references for the Methods section

51. Hassler, B. & Young, P. J. *Scientific Assessment of Ozone Depletion: 2022. Chapter 3: Update on Global Ozone: Past, Present, and Future*. 509 (2022).
52. Chipperfield, M. P. & Santee, M. L. *Scientific Assessment of Ozone Depletion: 2022. Chapter 4: Polar Stratospheric Ozone: Past, Present & Future*. 509 (2022).
53. Solomon, S. Stratospheric ozone depletion: A review of concepts and history. *Reviews of geophysics* **37**, 275–316 (1999).
54. Domeisen, D. I. V., Garfinkel, C. I. & Butler, A. H. The Teleconnection of El Niño Southern Oscillation to the Stratosphere. *Reviews of Geophysics* **57**, 5–47 (2019).
55. Lin, J. & Qian, T. A New Picture of the Global Impacts of El Nino-Southern Oscillation. *Scientific Reports* **9**, 17543 (2019).
56. Thompson, D. W. J. & Solomon, S. Interpretation of Recent Southern Hemisphere Climate Change. *Science* **296**, 895–899 (2002).
57. Wills, R. C. J. *et al.* Forced Component Estimation Statistical Method Intercomparison Project (ForceSMIP). *Journal of Climate* e250326 (2026) doi:10.1175/JCLI-D-25-0326.1.
58. Kostov, Y. *et al.* Fast and slow responses of Southern Ocean sea surface temperature to SAM in coupled climate models. *Climate Dynamics* **48**, 1595–1609 (2017).

59. Haarsma, R. J. *et al.* High Resolution Model Intercomparison Project (HighResMIP v1.0) for CMIP6. *Geoscientific Model Development* **9**, 4185–4208 (2016).
60. Hallberg, R. Using a resolution function to regulate parameterizations of oceanic mesoscale eddy effects. *Ocean Modelling* **72**, 92–103 (2013).
61. Kang, S. M. *et al.* Km-scale coupled simulation and model–observation SST trend discrepancy. *Proceedings of the National Academy of Sciences* **123**, e2522161123 (2026).
62. Zhou, C. *et al.* Sea ice pattern effect on Earth's energy budget is characterized by hemispheric asymmetry. *Science Advances* **11**, eadr4248.

Acknowledgments

We thank three anonymous reviewers for insightful and constructive feedback. P.W. gratefully acknowledges helpful discussions with Yue Dong and Vincent Cooper. We also thank Yue Dong, Bosong Zhang, and Chen Zhou for providing the Green's functions data. P.W. acknowledges support by the Stanford Science Fellowship. P.W. and S.S. acknowledge support from NSF-AGS grants 2316980. D.W.J.T. was supported by the National Aeronautics and Space Administration (NASA) under 80NSSC23K0113 and the National Science Foundation (NSF) under NSFGEO-NERC 2507587. N.S.D. acknowledges support from Stanford University. Parts of the computing for this project was performed on high-performance computing resources supported by the Stanford Research Computing Center and the Stanford Doerr School of Sustainability Center for Computation. We acknowledge the World Climate Research Programme, which, through its Working Group on Coupled Modelling, coordinated and promoted CMIP6. We thank

the climate modeling groups for producing and making available their model output, the Earth System Grid Federation (ESGF) for archiving the data and providing access, and the multiple funding agencies who support CMIP6 and ESGF.

Data Availability

CMIP6 PiControl, historical, SSP2-4.5, and HighResMIP model outputs are archived at the Earth System Grid Federation (https://aims2.llnl.gov/). COBE-SST2 is available from the NOAA Physical Sciences Laboratory (https://psl.noaa.gov/data/gridded/data.cobe2.html), ERSSTv6 is from the NOAA National Centers for Environmental Information (https://www.ncei.noaa.gov/products/extended-reconstructed-sst), and HadISST1 is from the U.K. Met Office (https://www.metoffice.gov.uk/hadobs/hadisst/). ForceSMIP SST data are available on Zenodo (https://doi.org/10.5281/zenodo.17106679). The SBUV ozone dataset is available from the NASA Goddard Space Flight Center (https://acd-ext.gsfc.nasa.gov/Data_services/merged/). All CMIP6 and observational SST datasets were re-gridded to a common horizontal resolution, and the re-gridded datasets are available at Zenodo (https://doi.org/10.5281/zenodo.19445924).

Code Availability

The code used to generate all of the figures in this analysis is available at Zenodo (https://doi.org/10.5281/zenodo.19445924).

Author Contributions

P.W. designed the study, analyzed the data, and drafted the initial manuscript. S.S., C.D., D.W.J.T., and N.S.D. contributed significantly to the interpretation of findings and revised the manuscript.

Competing Interests

The authors declare no competing interests.

Correspondence and requests for materials

Peidong Wang (pdwang@stanford.edu)

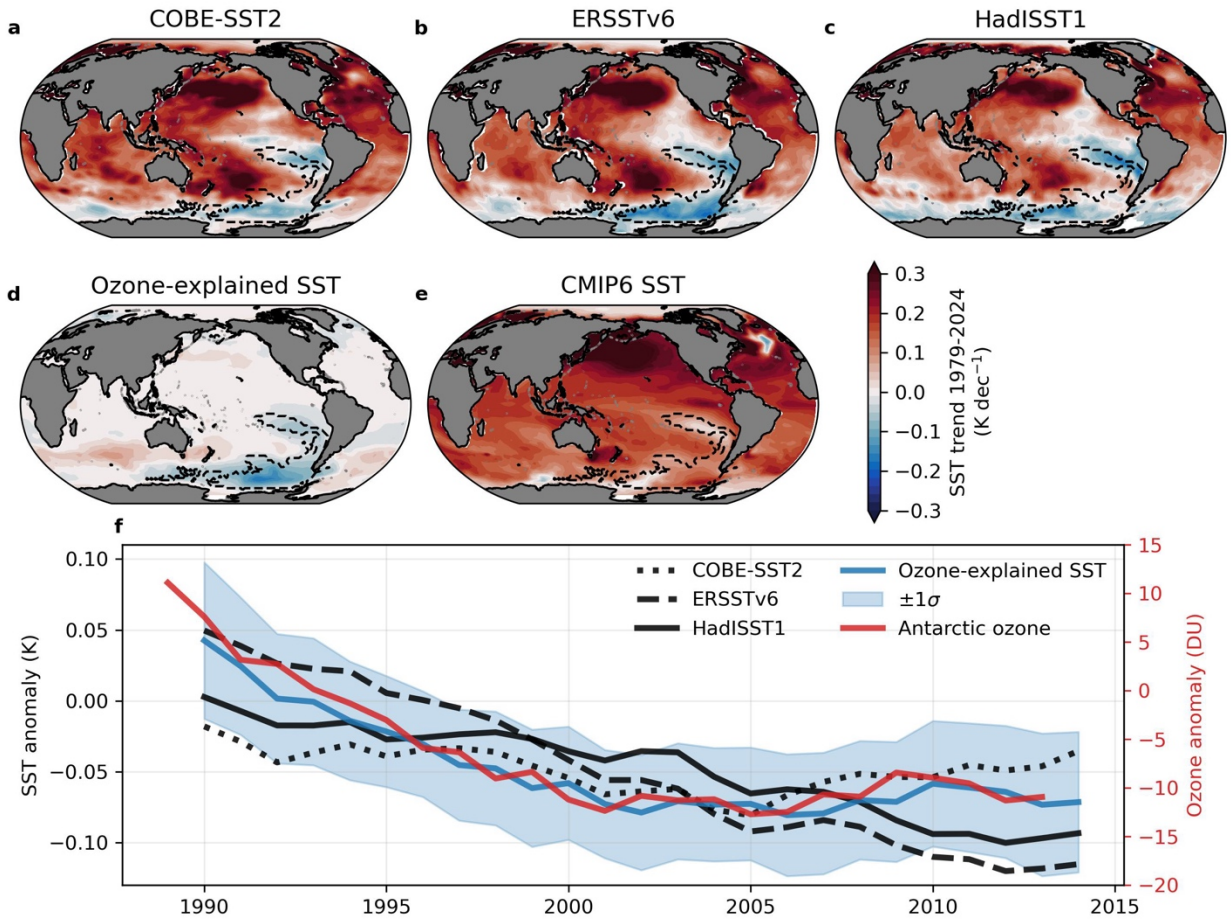

Figure 1. Comparison of observed and modeled sea surface temperature trends. Panels a-e show linear SST trend maps from 1979 to 2024. Panels a-c show observations from three SST datasets (COBE-SST2, ERSSTv6, and HadISST1, respectively). Panel d shows the multi-model-mean ozone-explained SST from the MLR based on eight GCMs (Extended Data Table 1). Panel e shows the multi-model-mean direct SST output from the same eight GCMs. Panel f shows 22-year running-mean SST anomalies averaged over the eastern tropical Pacific and Southern Ocean (region enclosed by the dashed contours in a-e where all eight GCMs agree in the sign of the ozone-induced SST response). Black (solid, dashed, and dotted) curves denote three different SST observations, the blue curve shows the MLR-predicted SST with ±1σ shading indicating uncertainties from regression coefficients, and the red curve (right y-axis) shows the 22-year running-mean September-December total column ozone anomaly from the SBUV observations, averaged over 60°S-90°S.

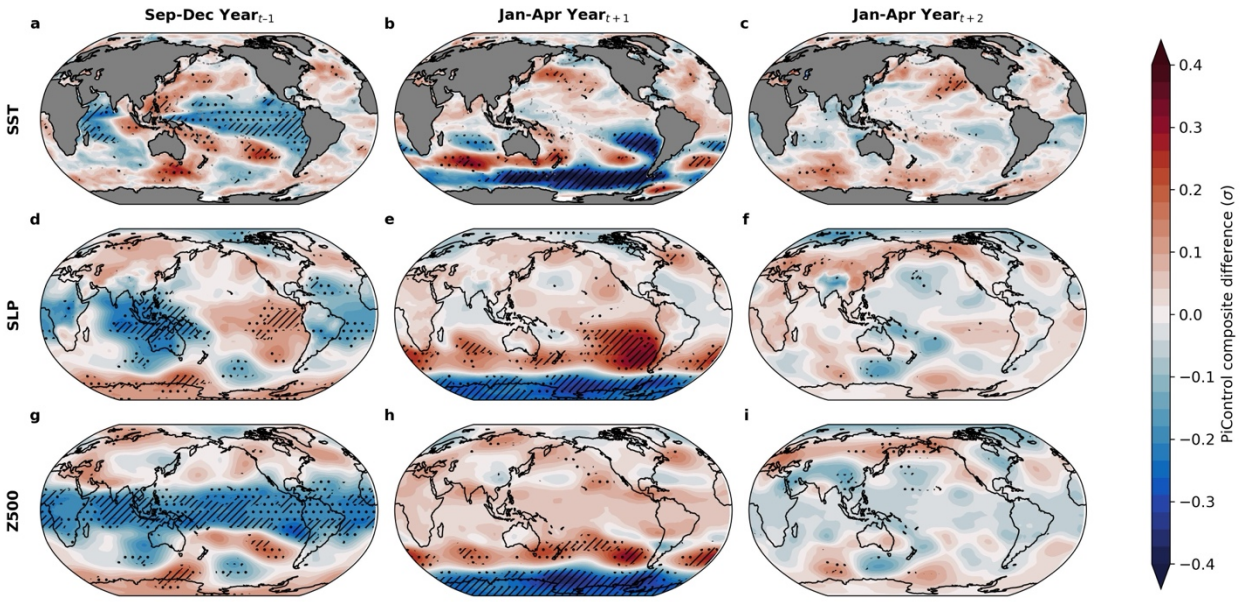

693

694 **Figure 2. Composite sea surface temperature and atmospheric circulation**
695 **anomalies associated with low Antarctic ozone.** Panels a-i show multi-model-mean
696 composite differences between low Antarctic ozone years (<10th percentile) and moderate
697 Antarctic ozone years (40th-60th percentile) in the eight CMIP6 PiControl simulations.
698 Differences in SST (a,b,c), SLP (d,e,f), and Z500 (g,h,i) are shown for the austral spring
699 one year prior to low Antarctic ozone (a,d,g), the subsequent austral summer (b,e,h), and
700 the austral summer two years later (c,f,i). Each field is normalized by its own standard
701 deviation within each GCM's PiControl run before averaging across the eight GCMs,
702 resulting in anomalies in units of σ. Hatching indicates regions where all eight GCMs
703 agree on sign, and dots mark regions where seven of eight GCMs agree on sign.

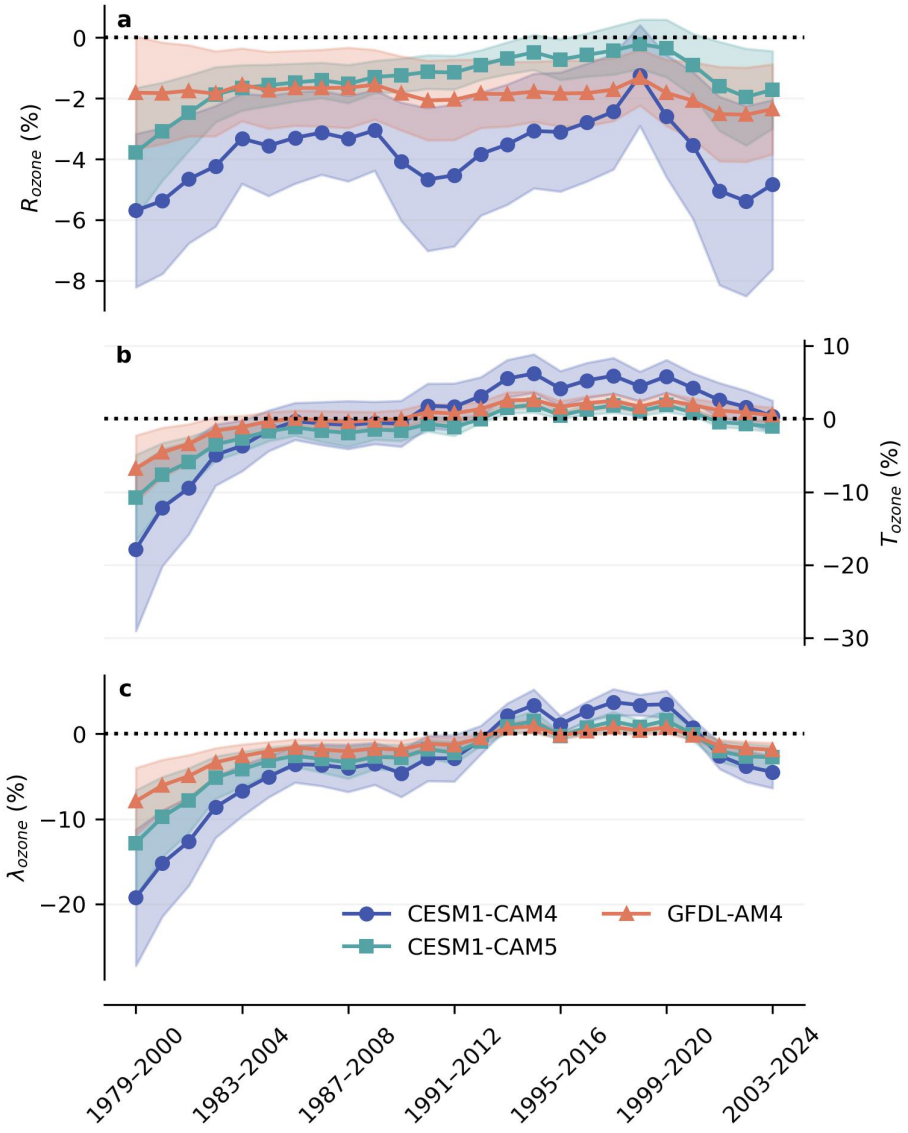

Figure 3. Climate sensitivity due to ozone-induced sea surface temperature pattern changes. Panel a shows percent difference in top-of-atmosphere net radiation *R*, panel b in global-mean surface temperature *T*, and panel c in global radiative feedback parameter *λ*, each estimated using the Green's function between observed SST and its counterpart with the ozone-explained SST removed. Accordingly, these percent differences quantify the contribution of ozone-induced SST pattern changes in *R*, *T*, and *λ*. Results are calculated over sliding 22-year trend windows from 1979 to 2024. Each color represents a different Green's function; the solid curve shows the mean estimate, and the shading denotes the ±1σ uncertainty arising from the spread across the three observational SST products and the uncertainty in the MLR regression coefficients.

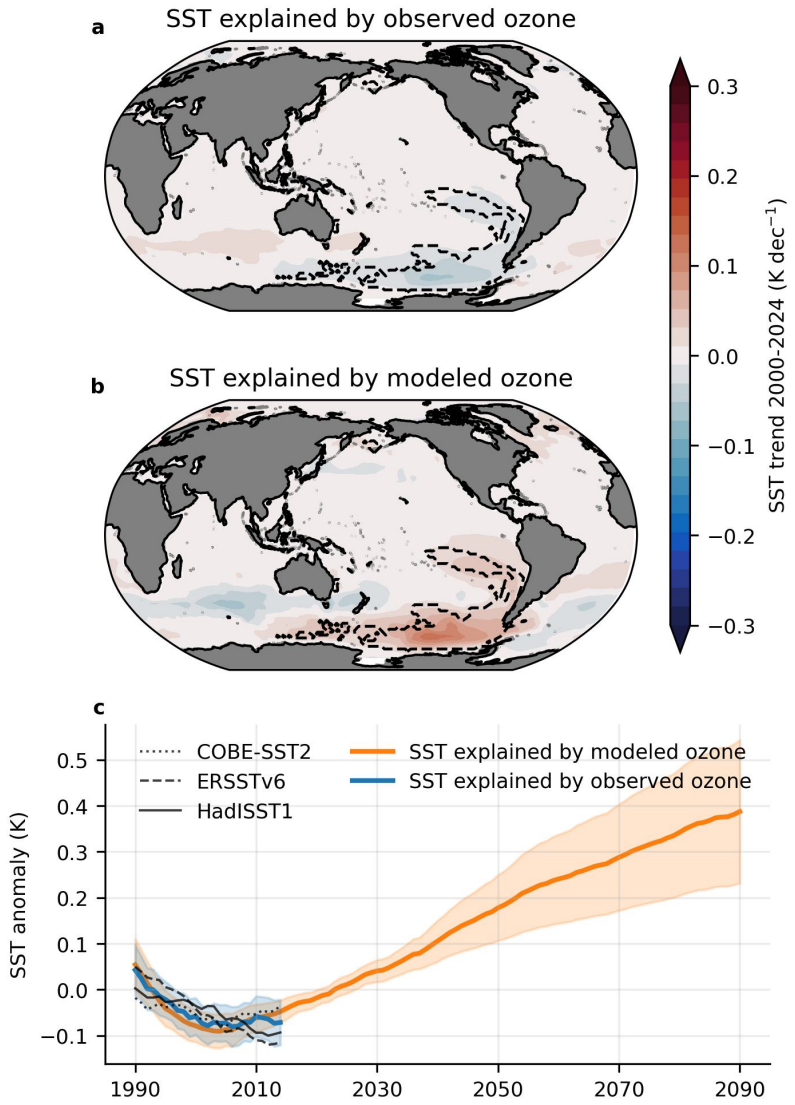

Figure 4. Comparison of ozone-explained sea surface temperature using observed and model-simulated ozone. Panels a and b show SST trend maps from 2000 to 2024 derived from the MLR using observed ozone from SBUV and simulated ozone from CMIP6 (with historical simulations prior to 2014 and SSP2-4.5 thereafter), respectively. Panel c shows 22-year running-mean SST anomalies averaged over the eastern tropical Pacific and Southern Ocean (region enclosed by the dashed contours in a-b). Blue and orange curves denote SST driven by SBUV and CMIP6 ozone, respectively, with shading indicating ±1σ from the MLR regression coefficients. Black solid, dashed, and dotted curves show the three SST observation products for comparison. The blue and black curves in c are identical to those shown in Figure 1f.

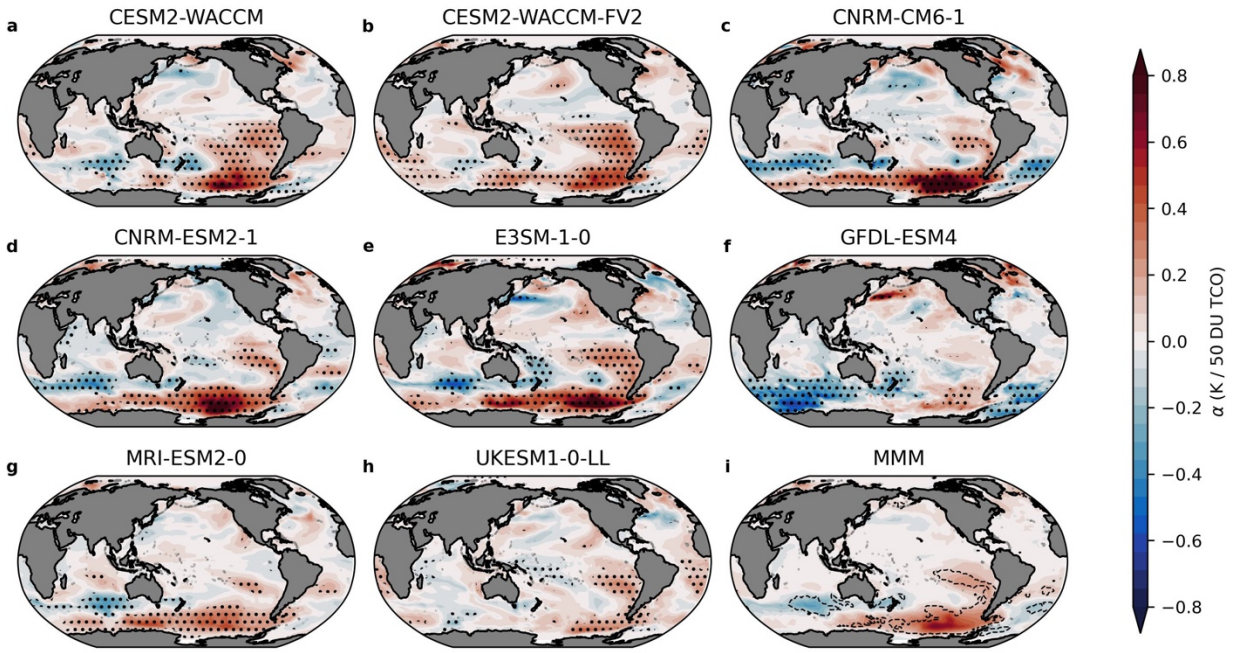

Extended Data Figure 1. Regression coefficients on Antarctic ozone in the MLR. Panels a-h show partial regression coefficients on Antarctic ozone for individual CMIP6 GCMs derived from their PiControl simulations. Dots indicate regions where the $p < 0.05$ in the MLR, denoting higher confidence in the SST response to Antarctic ozone. Panel i shows the multi-model-mean of the regression coefficients, with dashed contours highlighting regions where all eight GCMs agree on the sign of the SST response to Antarctic ozone.

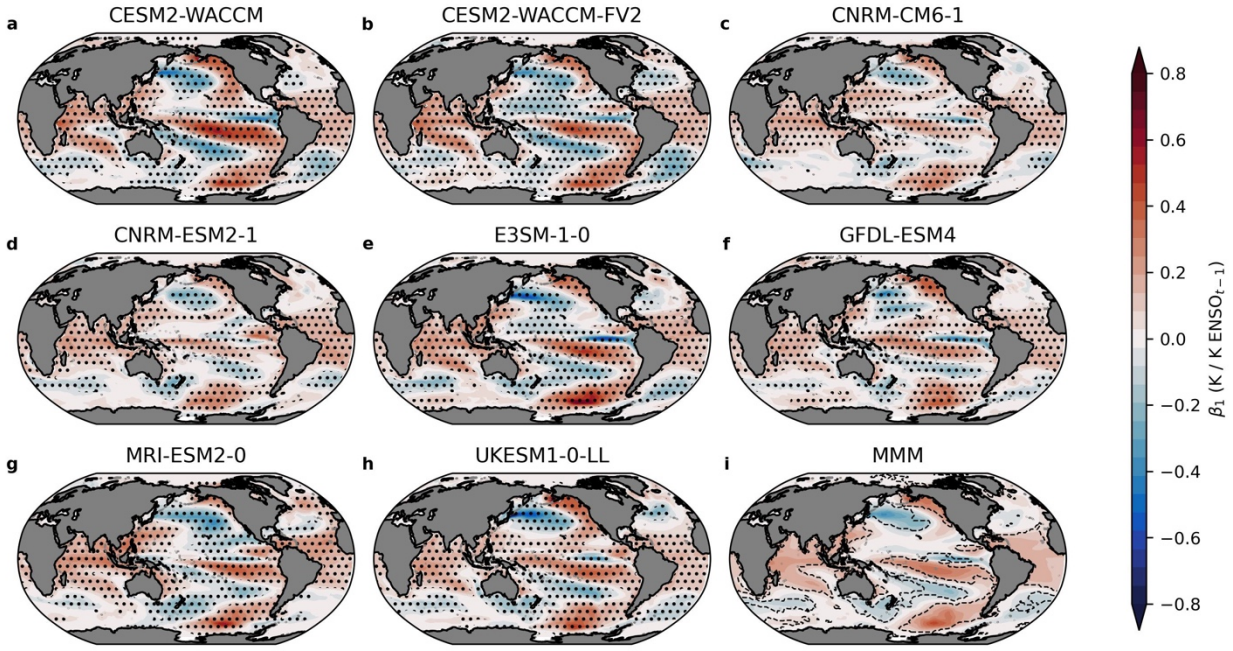

734

735 **Extended Data Figure 2. Regression coefficients on ENSO (lag 1-year) in the MLR.**

736 Same as Extended Data Figure 1, but for ENSO with a 1-year lag.

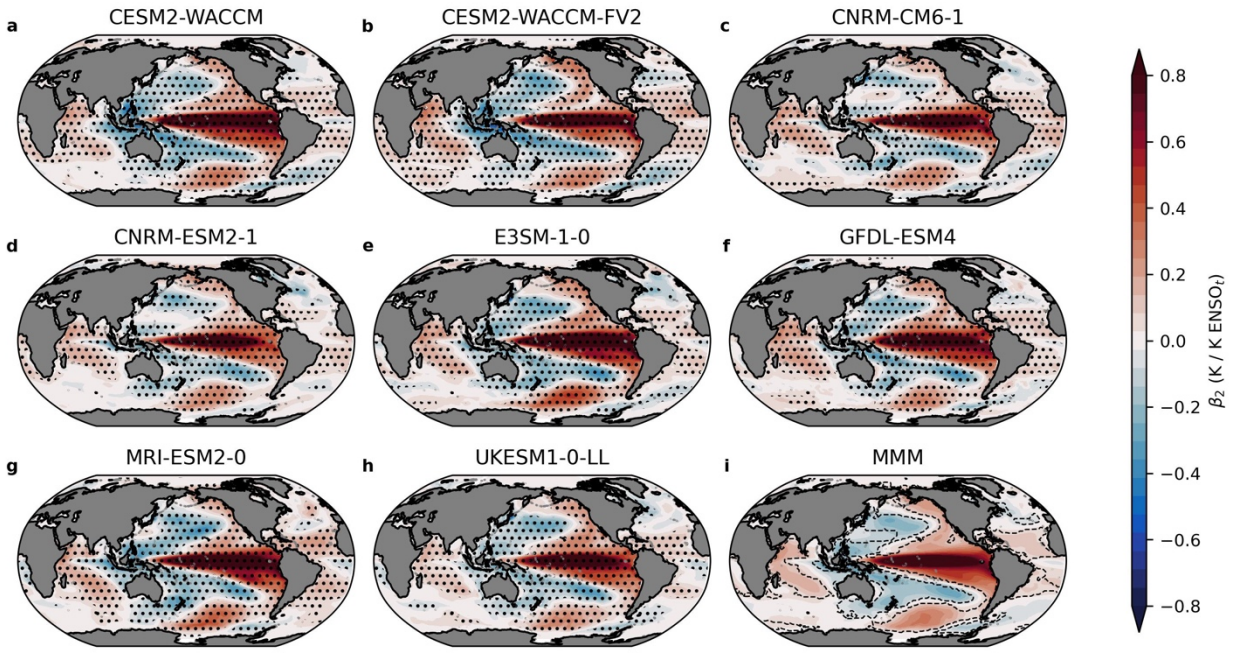

737

738 **Extended Data Figure 3. Regression coefficients on ENSO (lag 0-year) in the MLR.**

739 Same as Extended Data Figure 1, but for ENSO with a 0-year lag.

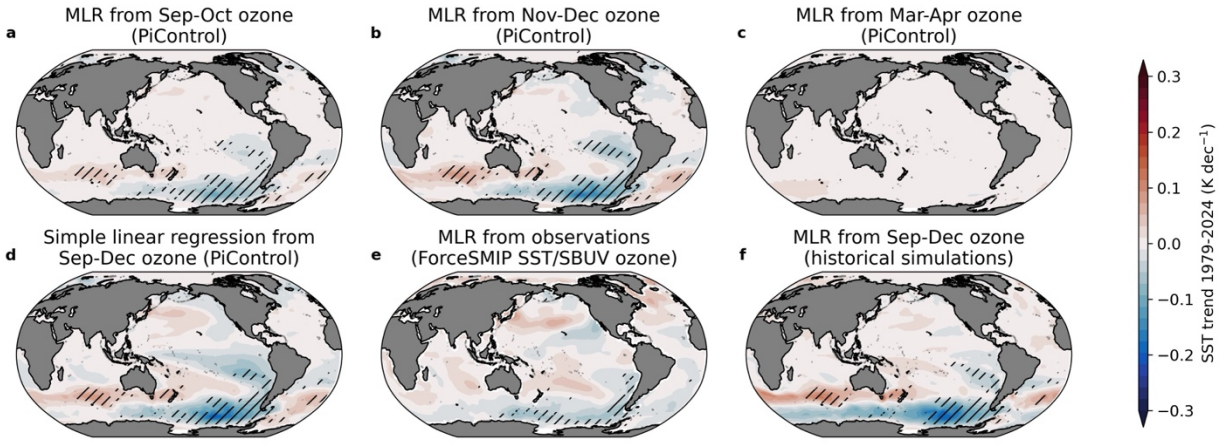

Extended Data Figure 4. Sea surface temperature trends from linear regression sensitivity tests. Panels a-c show SST trends during 1979-2024 derived from MLR using Antarctic ozone (60°S-90°S) averaged over September-October, November-December, and March-April, respectively. Panel d shows SST trends derived from a simple linear regression using Antarctic ozone as the sole predictor (without including ENSO indices). Panels a-d are based on the multi-model mean of the regression coefficients from the eight CMIP6 PiControl simulations. Panel e shows the SST trend based on MLR using September-December Antarctic ozone constructed from observations during 1979-2022, with SST data from ERSST after subtracting the forced component estimated from ForceSMIP. Panel f shows the mean SST trend based on MLR using September-December Antarctic ozone constructed from internal variability in historical simulations during 1975-2014 for CNRM-CM6-1, CNRM-ESM2-1, MRI-ESM2-0, and UKESM1-0-LL. Hatching in regions where all eight PiControl regression coefficients agree on the sign of the response (dashed region in Extended Data Figure 1i) indicates where SST trends from these sensitivity tests lie within ±1σ of the multi-model mean SST trend predicted by the PiControl MLR (Figure 1d).

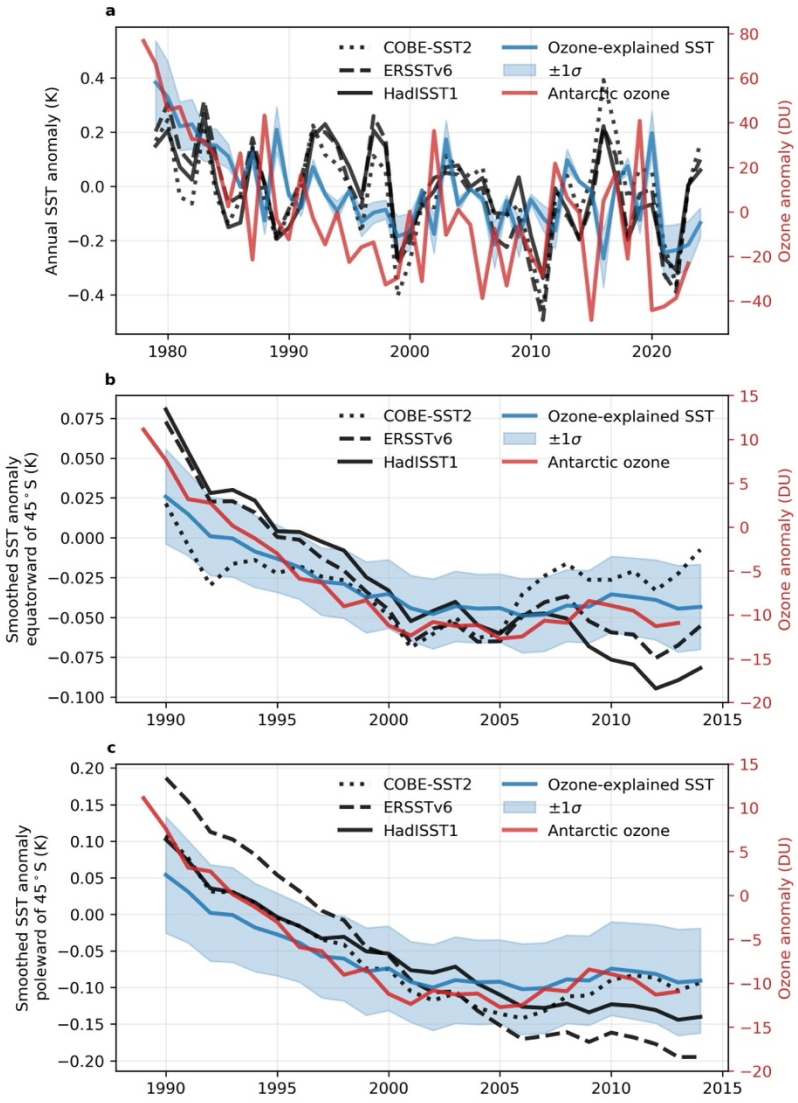

Extended Data Figure 5. Sea surface temperature anomalies on interannual timescales and regional averages. Panel a is the same as Figure 1f but without the 22-year running mean. Panels b and c are the same as Figure 1f but show the 22-year running-mean SST anomalies averaged separately over the eastern tropical Pacific (equatorward of 45°S) and the Southern Ocean (poleward of 45°S), respectively.

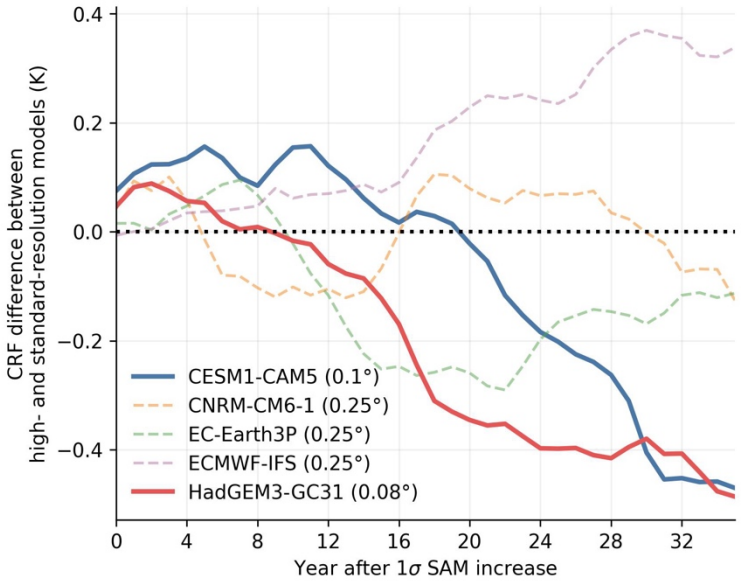

Extended Data Figure 6. Climate response function differences between high- and standard-resolution ocean models. CRFs for Southern Ocean SST in response to SAM increases are calculated from HighResMIP models with paired high- and standard-resolution configurations. The difference between the high- and standard-resolution CRFs is plotted, illustrating how the SST response changes with increased model resolution. The horizontal resolution of the high-resolution ocean configuration is indicated in the legend for each GCM. The two GCMs with ocean resolutions finer than 0.1° (minimum resolution required to fully resolve mesoscale ocean eddies) are shown with solid curves, whereas the three GCMs with 0.25° ocean resolution are shown with lighter dashed curves, as this resolution may still be too coarse to fully resolve mesoscale ocean eddies.

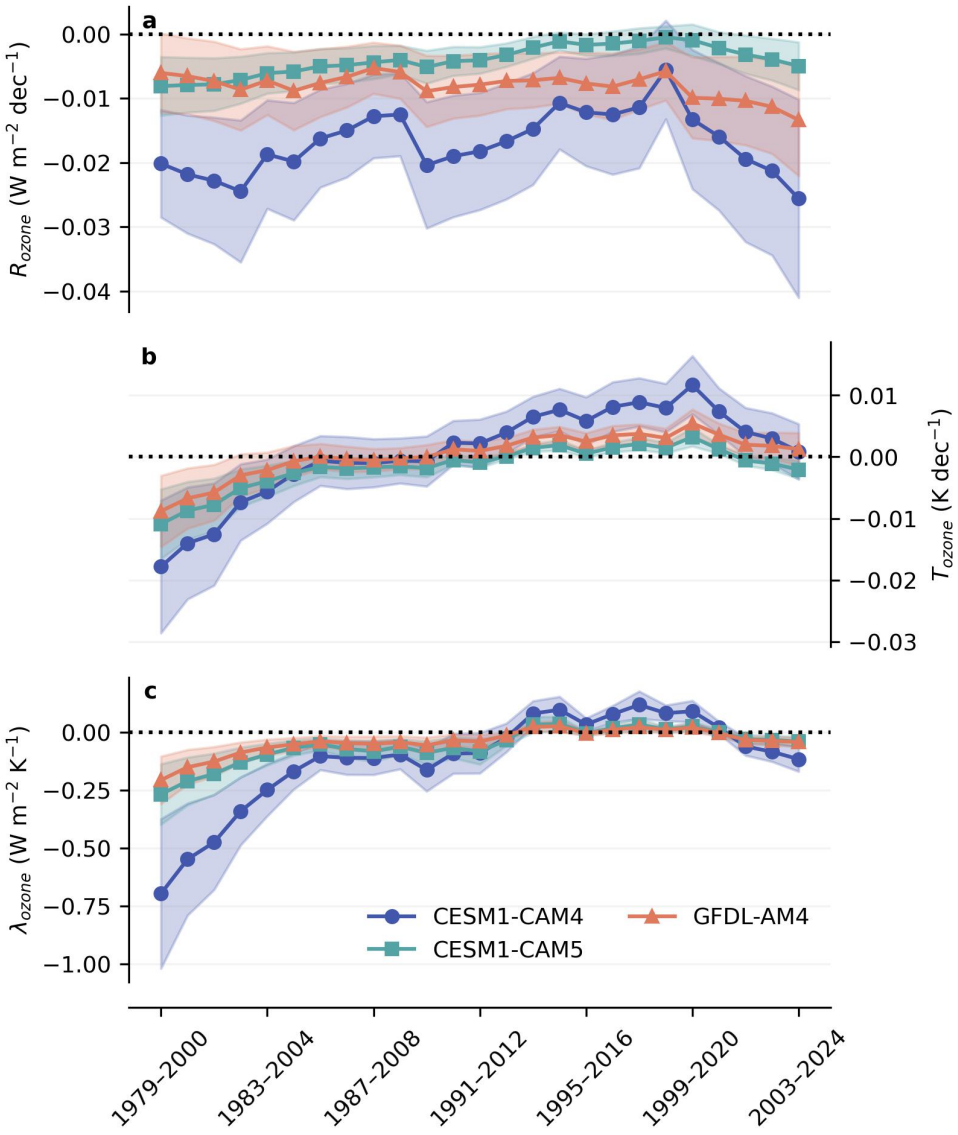

774

775 **Extended Data Figure 7. Climate sensitivity associated with different sea surface**
776 **temperature trend patterns.** Same as Figure 3, but in absolute values.

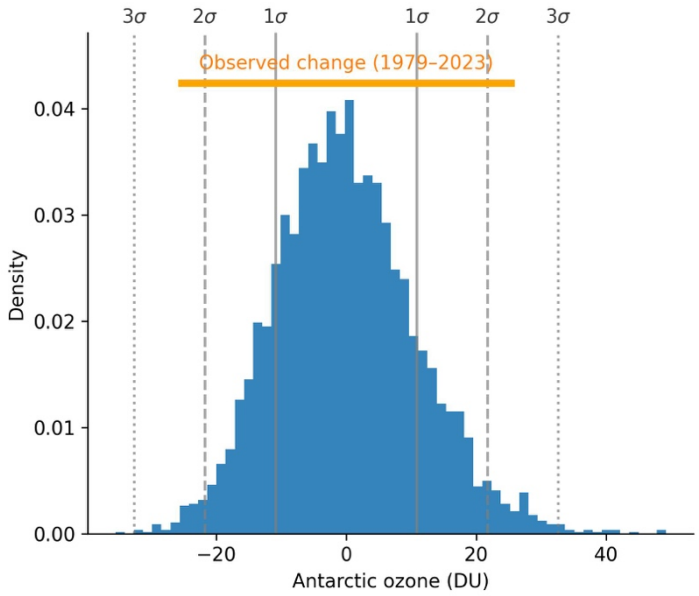

Extended Data Figure 8. Comparison of Antarctic ozone variability between PiControl simulations and observations. The histogram shows the distribution of September-December polar-cap (60°S-90°S) total column ozone anomalies in PiControl simulations from the eight CMIP6 GCMs considered in this study. The vertical gray solid, dashed, and dotted lines indicate the ±1σ, ±2σ, and ±3σ ranges of PiControl variability, respectively. The horizontal yellow bar indicates the total change in ozone from SBUV satellite observations during 1979-2023. The observed Antarctic ozone change during the past four decades generally falls within the ±2σ to ±3σ range of ozone variability in the PiControl simulations.

Extended Data Table 1. List of CMIP6 GCMs used in this study.

Model	Years of PiControl used to construct MLR	Historical and SSP availability	Stratospheric ozone
CESM2-WACCM	499	Historical+SSP2-4.5	Fully interactive
CESM2-WACCM-FV2		Historical	Fully interactive
CNRM-CM6-1		Historical+SSP2-4.5	Linearized scheme
CNRM-ESM2-1		Historical+SSP2-4.5	Fully interactive
E3SM-1-0		Historical	Linearized scheme
GFDL-ESM4		Historical+SSP2-4.5	Fully interactive
MRI-ESM2-0		Historical+SSP2-4.5	Fully interactive
UKESM1-0-LL		Historical+SSP2-4.5	Fully interactive